Large-Eddy Simulation of Roll Structures in the Marine Boundary Layer

A. Chlond

Max-Planck-Institut für Meteorologie, Hamburg

1. Introduction

Boundary layer clouds are an important component of the climate system since they cover about a quarter of the Earth; they have a strong influence on atmosphere-ocean coupling, they are also a major factor in determining the Earth's radiation budget by reflecting incoming solar radiation and absorbing upwelling terrestrial radiation and last but not least might take part in climate change. Slingo (1990) calculated that even modest relative increases of 15-20% in the amount of low clouds and 20-35% in liquid water path, and a decrease of 15-20% in mean drop radius can balance the top of the atmosphere radiative forcing by doubled carbon dioxide concentrations. However, our present understanding is insufficient to reliable predict how clouds respond to climatic perturbations so that their potential for amplifying or damping trace gas induced climate change remains one of the greatest challenges for atmospheric research.

Hence, the goal of our work has been to investigate in detail the processes that control the formation and dissipation of boundary layer clouds and to provide a physical basis for a better representation of moist boundary layer processes in general circulation models. The approach undertaken is to use a LES (Large-Eddy Simulation) model that incorporates a reasonably detailed description of the processes occurring in a moist boundary layer in order to investigate the influence of the boundary layer eddy structure on such clouds. Our study concentrates on the simulation of clouds and the boundary layer modification under convective conditions during cold air outbreaks where cold air from the polar ice caps or from the continents flows offshore over the relatively warm open waters. Preferred locations of cold air outbreaks are the Greenland Sea, Barents Sea and Bering Sea as well as the warm ocean currents on the east sides of the continents. Extensive cold air outbreaks typically cover areas

of about 10^6 km^2 and are associated with large sensible and latent heat transfers from the ocean to the atmosphere which can reach several 100 W/m^2 in extreme cases. Such weather episodes lead to the largest world wide air-sea energy exchanges and contribute substantially to the air-sea energy exchange in high and middle latitudes.

The cold and dry air from the ice or land surface is rapidly heated and moistened over the water. The initial, dynamically influenced character of the boundary layer changes to a convectively influenced one, resulting in an increase of boundary layer depth with increasing distance from the ice edge or coast. In most cases, cloud streets form 100 km or less downstream from the shore line and provide flow visualization of the flow patterns developing within the convective boundary layer. The conception is that the secondary flow consists of horizontal roll vortices which extend throughout the depth of the boundary layer. Their axis is roughly in the direction of the basic flow and parallel stripes of upward motion within these helical motions may in some cases be marked with clouds. In other cases, the rolls are indicated by rows of dense dark clouds within a solid cloud cover. The spacing between adjacent cloud lines is normally between 2 and 8 km and they persist for several hundred kilometres south of the ice edge where a transformation takes place to a three-dimensional cellular convective regime.

The conditions for the formation of these rolls have been the subject of many theoretical and observational studies, e.g. Küttner (1971), Le Mone (1973) and Brown (1980). The cause of the rolls has been attributed to both a shear instability of the Ekman planetary boundary layer and the organization of buoyant convection by velocity shear. Often it is a combination of these two instability mechanisms. A number of observational studies of cloud street formation during cold air outbreaks (Walter, 1980; Miura, 1986) have provided information as to how the interval between the cloud lines changes with distance south of the edge of the ice pack, but not on turbulent and roll-scale transports of momentum and energy. Therefore, it might be useful to apply a numerical model to the cold air outbreak problem, with special emphasis on the boundary layer eddy structure and on turbulent statistics.

The observed two-dimensionality has formed the basis for several numerical studies, e.g. Mason and Sykes (1982), Mason (1985), Etling and Raasch (1987), Chlond (1987), Sykes et al. (1988, 1990), and Raasch (1990). These studies have provided a better understanding of the physical processes involved, and have given a detailed information on roll-scale velocity variances and roll-scale vertical transports. However, since the models used have assumed homogeneous conditions in the direction of the roll axis, they cannot predict whether two-dimensional eddies should actually dominate the flow. In addition, calculations by Chlond (1987) lead to the suggestion that the relation between the cross-roll and along-roll velocity variances cannot be

reproduced in the right manner by two-dimensional models.

Therefore, we try to extend this work. Unlike previous studies of the moist convective boundary layer, which were subject to limitations in the ability to resolve the actual eddy structure, our primary interest here is in simulating the temporal development of three-dimensional boundary layer flows during cold air outbreaks under conditions where the surface heat flux, latent heat release and radiative fluxes should have a strong effect. Hence, a three-dimensional numerical model has been developed in order to fully take into account circulations acting in both horizontal and the vertical plane. The general idea underlying the model is that of a large-eddy model. The model explicitly calculates the spatial averages, which hopefully represent the dominant large-scale motions, while parameterizing the effect of the fluctuations on the averaged flow quantities. The model is applied to conditions corresponding to an observed case of cloud street/stratocumulus development which occurred over the Greenland Sea during the ARKTIS 1988 experiment (Brümmer et al., 1992). Our principal objectives are to determine the respective roles of condensation, cloud top radiative cooling, large-scale subsidence, the large-scale moisture field and time dependent surface heating on the boundary layer rolls by considering simulations with and without these effects. Although the model is far from being perfect for the simulation of such complex boundary layer phenomena, it can give at least some insight into the exchange process between ocean and atmosphere due to organized vortices in the boundary layer.

The paper proceeds as follows. In Section 2 we describe the large eddy simulated cases. Section 3 presents results obtained with a series of 3 h simulations for conditions commonly observed during cold air outbreaks. We will report on the information the model yields concerning the influence of the various physical processes and external parameters on the roll development. Qualitative and quantitative descriptions of the flow field are given. Additionally, vertical profiles of mean wind, virtual potential temperature, specific humidity, liquid water content, radiative cooling, turbulent and roll-scale variances and fluxes as well as roll-scale energy production terms are presented. Finally, the conclusions are summarized in Section 4.

2. *The large-eddy simulations*

The results presented below were obtained using the three-dimensional model described by Chlond (1992). The basic dynamic frame-work of our model follows that of a large-eddy simulation (LES) model. The basic idea of large-eddy modelling is to isolate the dynamics of the dominant large-scale motions, while parameterizing the effects of the small scales on the averaged flow quantities. This approach hinges on the hypothesis that the actual details of the subgrid model have only minor effects

on the large scale. The LES approach was first applied to meteorological flows by Deardorff (1972) and Sommeria (1976); it is discussed and reviewed by Herring (1979) and Schumann and Friedrich (1986).

Briefly, this is a finite-difference model with second-order accurate differencing in space and time of the incompressible Boussinesq equations for motion. The model is formulated using primitive variables, i.e., the three velocity components are integrated foreward in time, and an elliptic equation for pressure is solved at each time step to ensure conservation of mass. The thermodynamics are represented by conservation equations for liquid water potential temperature and total moisture content. These variables are chosen for their conservation properties during phase changes of water. The model includes most of the physical processes occurring in a moist boundary layer in the absence of precipitation. It contains a water cycle (using the partial cloudiness formulation of Sommeria and Deardorff, 1977); it takes into account infrared radiative cooling (following the parameterization of Stephens, 1978) and the influence of large-scale vertical motions. The subgrid flux model is based on a transport equation for the subgrid-scale turbulent kinetic energy and is similar to that of Deardorff (1980), and Sykes et al. (1988).

A series of simulations have been carried out in order to demonstrate the model's ability to serve as a tool to interpret experimental data and to understand the various physical processes acting in a cloudy convective boundary layer during a cold-air outbreak. These simulations used 64 x 64 x 32 grid points covering a numerical domain of 6.4 km x 6.4 km x 1.6 km. Therefore, they resolve turbulent eddies of sizes down to 200 m x 200 m x 100 m, twice the grid spacing.

Firstly, the model is applied to conditions corresponding to an observed case of cloud street / stratocumulus development which occurred over the Greenland Sea during the ARKTIS 1988 experiment. The experiment took place in the Fram Strait in the area straddling the ice margin west of Spitsbergen during the period from 5 to 27 May 1988. The experiment was dedicated to the study of boundary layer modification and certain cloud structures in cases of off-ice and on-ice air flows.

To set up the case study which serves as a control run we have to define the geographical latitude, the boundary conditions, the external parameters which characterize the large-scale field, and to specify the initial conditions for all prognostic variables. The parameters and the boundary layer profiles have been selected in agreement with the main features observed during the period 1630-1900 UTC on 16th May 1988 in the ARKTIS experiment (Brümmer et al., 1992). During this period, a northerly wind in the boundary layer caused cold air to flow off the ice pack over relatively warm water, where the PBL was quickly modified. Cloud streets are formed 40 km or less downstream from the coastline. The cloud layer thickens quite

rapidly with the downwind distance from the coast and forms a near closed cloud layer at a distance of about 100 km from the ice edge, in which the rolls can be identified as rows of dense dark clouds. Both the air temperature and the water vapour mixing ratio increase downstream at a rate of about 3.5K per 200 km and 0.4 g/kg per 200 km, respectively. The water temperature field exhibits a rather complex structure. However, there is a general tendency for increasing sea surface temperatures towards the southwest. The boundary layer thickens in the downwind direction but additionally shows a crosswind inclination from northwest to southeast. Wind speeds are between 10 and 18 m/s.

We are now considering the idealized problem of a geostrophic wind blowing out about 45° with 25 m/s. An east-west oriented infinite straight coastline separates the ice pack from the ocean with surface temperature varying normal to the coast, but uniform parallel to the coast. The model is driven by time-varying, uniform surface boundary conditions and a geostrophic wind parallel to the y-axis. In comparing with observations, we note that the computational domain is translating with a fixed speed along the geostrophic wind direction. Thus, with a geostrophic wind speed of 25 m/s and an angle of 45° between the coastline and the geostrophic wind direction 1 hour of integration time corresponds to a travelling distance of about 64 km normal to the coastline. The latitude has been taken to be 79°N. At the shoreline the lower boundary condition corresponds to an oceanic surface at 272.16 K at saturation ($\overline{q} = 3.6 \cdot 10^{-3}$), and where the roughness lengths are equal to 10^{-3} m. The temporal temperature variation of the ocean surface has been chosen equal to $1.875 \cdot 10^{-4}$ K s^{-1}, which corresponds to a spatial variation at a rate of $1.06 \cdot 10^{-2}$ K km^{-1}. The initial conditions, cloudless and horizontally homogeneous, have been prescribed as follows: Except for a superadiabatic surface layer, the initial atmosphere was stably stratified with a lapse rate of $\Gamma_{\overline{\Theta}l} = 8.88 \cdot 10^{-3}$ Km^{-1}. A $\overline{\Delta\Theta}l = 5$ K difference has been chosen between the temperature at the ocean surface and the first model grid point above the surface at $z = z_1 = 25$ m. The initial moisture profile shows a strong drop in specific humidity from saturation ($\overline{q} = 3.6 \cdot 10^{-3}$) at the surface to a constant value of $2.2 \cdot 10^{-3}$ above (i.e. $\overline{\Delta q} = 1.4 \cdot 10^{-3}$ and $\Gamma_q = 0$). With these values, the initial windprofile is obtained by running a one-dimensional version of the model to steady state. During this phase, temperature and humidity profiles are fixed. In order to drive the system this horizontally homogeneous solution is then transferred to the three-dimensional domain and perturbed by imposing small random perturbations on the temperature field at the first time step. The values of the input parameters for the case study (control run) are summarized in Table 1.

Table 1: Input parameters for the control run.

$f = 1.428 \cdot 10^{-4} s^{-1}$	$z_o = z_T = 10^{-3} m$
$u_g = 0 \quad v_g = 25\ m\ s^{-1}$	$\bar{\Theta}_l\ (z = z_T\ ,\ t = 0) = 272.16\ K$
$\bar{q}\,(z = z_T\ ,\ t = 0) = 3.6 \cdot 10^{-3}$	$\Delta\bar{\Theta}_l\ (t = 0) = 5K$
$\Delta\bar{q}\,(t = 0) = 1.4 \cdot 10^{-3}$	$\Gamma_{\Theta l} = 8.888 \cdot 10^{-3} K m^{-1}$
$\Gamma_q = 0 m^{-1}$	$\left(\frac{\partial\bar{\Theta}_l}{\partial t}\right)_{z = z_T} = 1.875 \cdot 10^{-4} K s^{-1}$
$\left(\frac{\partial\bar{q}}{\partial t}\right)_{z = z_T} = \left(\frac{\partial q}{\partial T}\right)^{SAT} \cdot \left(\frac{\partial\bar{\Theta}_l}{\partial t}\right)_{z = z_T}$	$F^{\downarrow}(z_{TOP}) = B(0) - 100W$

Secondly, five sensitivity simulations were performed to clarify the influence of various physical processes and external parameters on the development of coherent structures within the convective boundary layer. Our principal objectives are to determine the respective roles of a mean subsidence, a time dependent surface heating, a large scale moisture field, cloud top radiative cooling and latent heat release on the boundary layer modification by considering simulations with and without these effects. The sensitivity runs (1) to (3) were different in that one of the external parameters given in Table 1 is varied while the others are fixed. In this way we investigate the influence of a large-scale mean subsidence (Run 1 with w_{LS} = - 10^{-2} ms^{-1} at z = z_{TOP} = 1600 m), a time dependent surface heating (Run 2 with $(\partial\bar{\Theta}_l/\partial t)_{z=z_T} = 0$), and a large scale moisture field (Run 3 with Γ_q = -1.074 • 10^{-6}). Run (4) and (5) use the same external parameters as the control Run. Run (4) has no cloud top cooling whilst Run (5) artificially suppresses latent heat release. In Run 1 a linear profile of the mean subsidence has been adopted, corresponding to a large-scale velocity divergence of 6.25 • 10^{-6} s^{-1}, independent of height. The decrease of the total moisture content with height in Run 3 corresponds to a drop in the relative humidity from about 90% at z = 25 m to about 20% at z = 1600 m.

The integrations run over 3600 time steps up to t = 10800 s. In the following results are presented for the first two hours of the integration period. The results later on differ from those at t = 7200 s as far as that the boundary layer and the cloud layer keep on growing but do not exhibit significantly different structures.

3. Results

3.1. Secondary flow structure

The flow fields provide an important indication of the nature of the resolved scale eddies. Figures 1-3 illustrate typical realizations of the secondary flow pattern in vertical and horizontal plan views at times t = 1800 s (corresponding to a distance from the coast line of about y_d = 32 km), t = 4500 s (y_d = 80 km) and t = 7200 s (y_d = 128 km), respectively. The figures show isopleths of the various fields, where, except for $\overline{q_l}$ horizontal averages have been removed. In addition, the quantities are normalized by using the maxima of the quantities occurring in the cross section. Solid and dashed lines represent, respectively, positive and negative deviations from the mean; the contour interval is 0.2. Figure 1 shows contours of the vertical component of the velocity field in vertical x-z cross sections located at y = 3200 m (left panel) and in horizontal x-y sections in the middle of the cloud layer (right panel) at times a) t = 1800 s (at the 350 m level), b) t = 4500 s (at the 400 m level), and c) t = 7200 s (at the 500 m level). Figures 2-3 represent vertical and horizontal cross sections for the variables $\overline{q_l}$, $\overline{\Theta_v}$ for the same levels and times as Figure 1.

At time zero, the model starts from the equilibrium mean fields already described, except for a small random disturbance applied to the temperature at the lowest level. Its amplitude increases by instability and the boundary layer is found to grow rapidly as the cold air flows off the ice over the relatively warm water. Coherent structures were identified in this boundary layer. The three-dimensional results show that after about 15 min, convection starts in the form of horizontal roll vortices. Figure 1a shows fields of the vertical velocity at t = 1800 s, a short time after the onset of convection. As seen in the x-y plane, the w-eddies are organized into distinct bands oriented about 50° to the left of the direction of the geostrophic wind. In comparing the alignment of the bands, with the wind direction, an angle of about 29° results (the arrows labelled "wind" in Figure 1 give the direction of the surface wind). The lateral wavelength of the bands of about 1300 m in a layer of depth 500 m gives an aspect ratio of the rolls of about 2.6. In the x-z cross-section, parts of a roll shaped circulation are seen, with alternating regions of up- and downdrafts. These structures are not steady in form or highly regular though rolls propagating in the direction normal to the bands are the dominant feature. The maximum amplitude of $\overline{w}$ occurs at z = 500 m which corresponds roughly to the height of the inversion base. In this height the largest shear is found in the lateral mean wind component which

CONTROL RUN

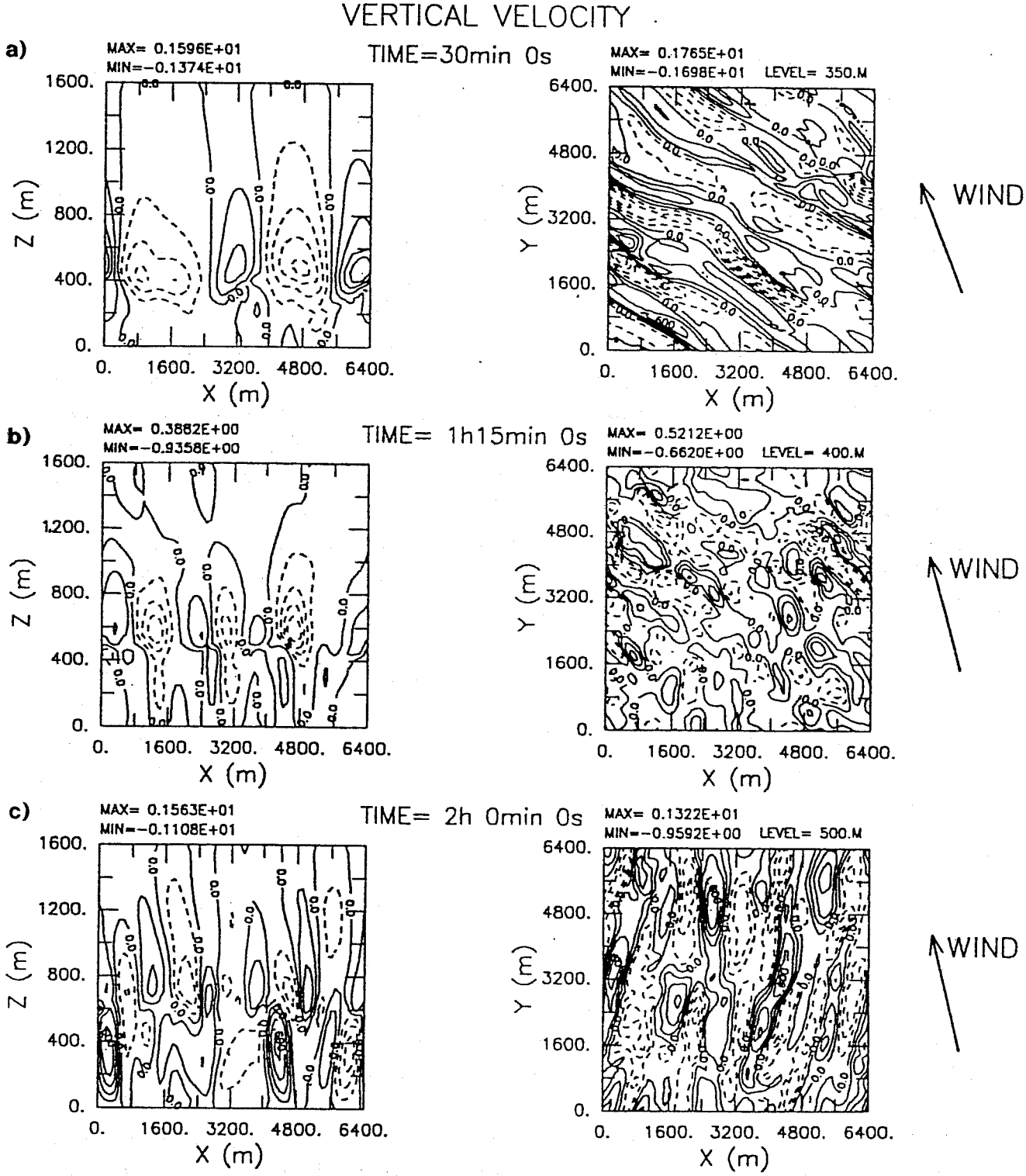

Fig.1: Contour plots of the vertical velocity in vertical x-z cross sections located at y = 3200 m (left panel) and in horizontal x-y planes (right panel) at times a) t = 1800 s (z = 350 m), b) t = 4500 s (z = 400 m) and c) t = 7200 s (z = 500 m) for the control run. Vertical velocity is normalized by using the maximum of this quantity occurring in the cross section (maximum indicated). Solid and dashed lines represent, respectively, positive and negative pertubations from the mean; the contour interval is 0.2.

CONTROL RUN

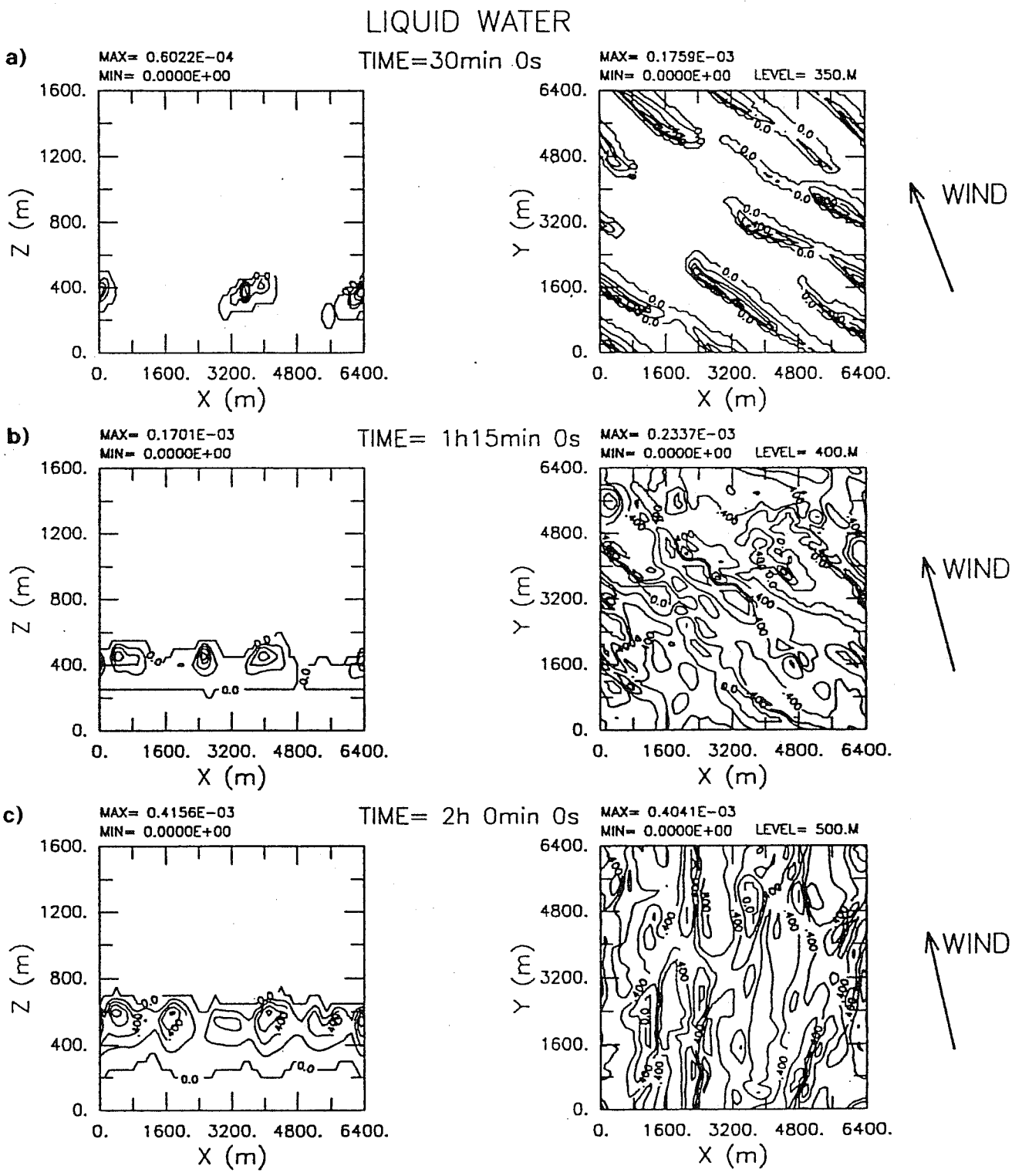

Fig.2: As Fig.1, except for the liquid water content.

CONTROL RUN

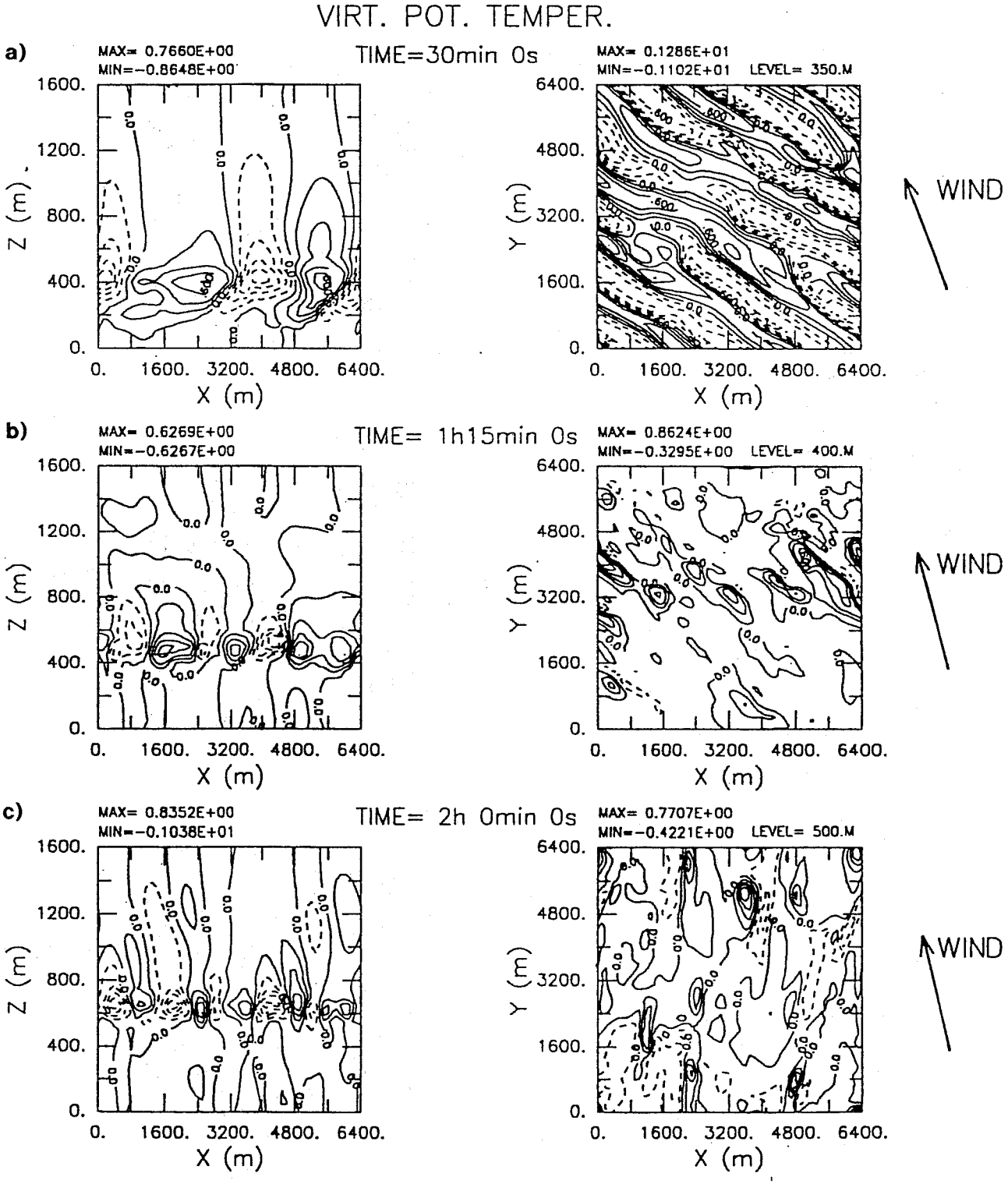

Fig.3: As Fig.1, except for the virtual potential temperature anomalies.

leads us to the asumption that these structures are related to a shear instability. The initial development in the form of elongated updrafts seems to break up after 1 hour of integration time. At t = 4500 s the w-eddies are more irregular and there is little evidence of any roll structure in this field. After 2 hours of integration time a reorganization of the vertical velocity field in the form of rolls is evident. The eddy elongation which does occur is close to the direction of the geostrophic wind, as shown in Figure 1c. This orientation coincides with values found by Mason and Sykes (1982) under unstable conditions. Most of the energy in the vertical velocity power spectrum is found at the 2.1 km wavelength which corresponds to a roll aspect ratio (wavelength / boundary layer height) of about 4 which is typical of rolls developing during cold air outbreaks at a greater distance from the shore line and corresponds to values reported by Brümmer et al. (1992). The maximum values of the $\overline{w}$-component are in the range between 1-2 m/s, and in agreement with experimental and theoretical results (Hein and Brown 1988; Brümmer et al., 1992; Raasch, 1990; Sykes et al., 1988, 1990). Note that now two centers of maximum vertical velocity occur. The secondary maximum is located at z = 700 m just above the inversion base and is associated with the strong shear in the lateral mean wind component. The primary maximum occurs at z = 350 m within the convective boundary layer indicating that the rolls become increasingly more convective in character with distance from the ice edge.

Figure 2 shows the liquid water field from the run, illustrating the initiation of clouds after about 1800 s, i.e. at a distance of about 32 km from the shoreline. The cloud layer thickens quite rapidly, and forms nearly a closed layer at t = 7200 s. The clouds, the word cloud referring to the region where $\overline{q_l}$ is positive, occur in a layer extending between 250 m and 750 m. The maximum liquid water content reaches 0.4 g/kg at t = 7200 s which seems to be reasonable for stratocumulus clouds. The cloud cover varies between 20% at t = 1800 s and 100% at t = 7200 s. The liquid water content does not exhibit a horizontal homogeneous structure but shows a clear positive correlation with the vertical velocity field, i.e. large values of $\overline{q_l}$ occur simultaneously with strong ascending motions whilst descending motions are characterized by small values of $\overline{q_l}$. In addition, penetrating updrafts cause an upwelling of the contours of constant liquid water content so that the cloud tops protude into the mean capping inversion. Therefore, cloud-top height, as well as cloud-base height is variable, typically over a 100 m height interval, within the context of the horizontal average. Simulated downstream variations of boundary layer heights and cloudiness over the open water are in rough agreement with the observations of Brümmer et al. (1992) but there seems to be an overprediction of mean cloud top heights.

The fields of virtual potential temperature shown in Figure 3 are seen to be well correlated with the field of the vertical velocity. At t = 1800 s the field of the vertical velocity is nearly at every level (except at the lowest two levels) out of phase with the

temperature perturbation field, i.e. maximum temperature perturbations coincide with strongest downward motions and vice versa, indicating conversion between roll kinetic energy and potential energy, resulting in a deepening of the boundary layer. At t = 4500 s and t = 7200 s the correlation between the $\overline{w}$- and $\overline{\Theta}_v$-fields is positive in the sub-cloud-layer and in the lower part of the cloud layer, indicating an upward buoyancy flux, and negative above. The temperature perturbation ($\overline{\Theta}_v$ - $<\overline{\Theta}_v>$) is determined largely by vertical advection of the mean temperature $<\overline{\Theta}v>$. Hence, large values of $\overline{\Theta}_v$ - $<\overline{\Theta}_v>$ were confined to the inversion layer, the region of strong gradients in $\overline{\Theta}_v$. Maximum temperature perturbations are found to be in the range between 0.5 - 1.5 K. A negative correlation between the two fields of virtual potential temperature and liquid water content near cloud top is also apparent. Virtual potential temperature is higher than the surrounding only in the lower part of the cloud layer and becomes appreciably lower in the upper part where evaporation of cloud droplets predominates.

3.2. Mean profiles

In this section we present vertical profiles of mean velocity components, virtual potential temperature, specific humidity, liquid water content, radiative cooling, profiles of total and resolved-scale variances of longitudinal momentum, lateral momentum and of vertical velocity, profiles of total and subgrid-scale transports of virtual potential temperature, moisture and shear stress profiles as well as resolved-scale energy production terms. Mean values over all points in one horizontal plane are denoted by brackets, e.g. $<\Psi> = <\Psi>(z)$ denotes a vertical mean profile of any quantity Ψ. Double primes denote local deviations from these mean values. For example Ψ'' represents $\Psi - <\Psi>$. Total variances and fluxes include resolved-scale and subgrid scale contributions, since, for example,

$$\langle \overline{u''^2} \rangle = \langle \overline{u}''^2 \rangle + \langle \overline{u'^2} \rangle$$

$$\langle \overline{w'' \Theta''}_v \rangle = \langle \overline{w}'' \overline{\Theta}''_v \rangle + \langle \overline{w' \Theta'}_v \rangle \ .$$

To obtain a compromise between statistical and local representation, the profiles were averaged over 100 time steps (5 min), at t = 1800 s and over 300 time steps (15 min) at t = 4500 s and t = 7200 s, respectively, corresponding to a time interval in which the boundary layer growth is less than 50 m.

Figures 4a-4f show mean boundary layer profiles of $<\overline{u}>$, $<\overline{v}>$, $<\overline{\Theta}_v>$, $<\overline{q}_v>$, $<\overline{q}_l>$ and $(\partial\overline{\Theta}_l/\partial t)_R$. Solid lines are used to denote the initial profiles and dashed line patterns

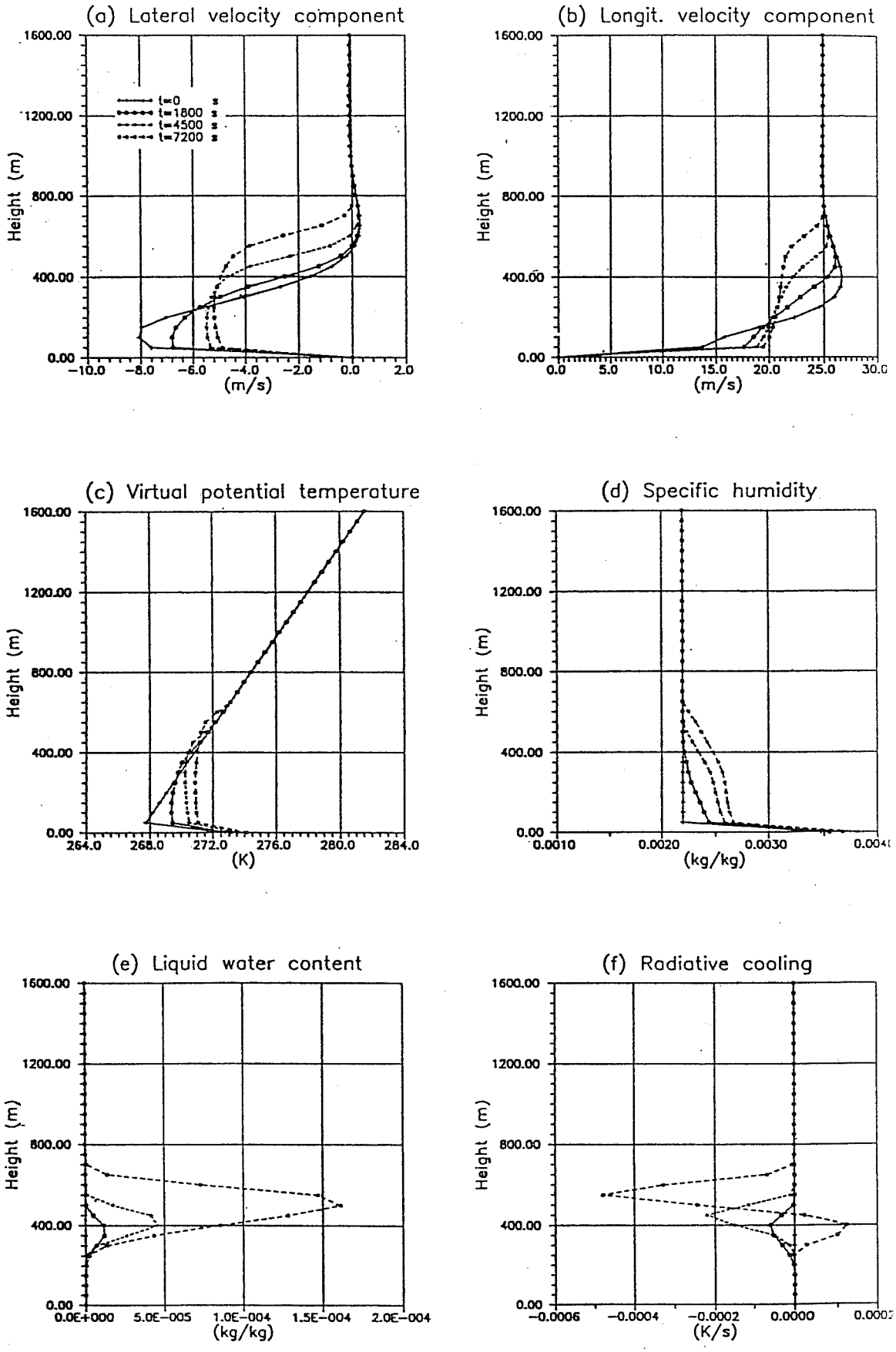

Fig.4: Vertical mean profiles of the lateral velocity component $\langle \bar{u} \rangle$ (a), of the longitudial velocity component $\langle \bar{v} \rangle$ (b), of the virtual potential temperature $\langle \bar{\theta}_v \rangle$ (c), of the specific humidity $\langle \bar{q}_v \rangle$ (d), of the liquid water content $\langle \bar{q}_l \rangle$ (e), and of radiative cooling $\langle (\partial \bar{\theta}_l / \partial t)_R \rangle$ (f) for the control run. Solid lines are used to denote the initial profiles, dashed line patterns to denote the profiles at t = 1800 s, t = 4500 s and at t = 7200 s, respectively.

to denote the profiles after 1800 s, 4500 s and after 7200 s of integration time, respectively. The initial longitudinal wind component $\langle\bar{v}\rangle$ is characterized by a weak maximum at z = 400 m and an inflection point may be noted in the lateral $\langle\bar{u}\rangle$-wind component at a height of about 350 m. The initial profile of virtual potential temperature $\langle\bar{\Theta}_v\rangle$ is characterized by a temperature difference between the ocean surface and the overlying air and a constant lapse rate above. Likewise, the initial humidity profile $\langle\bar{q}_v\rangle$ shows a humidity jump in the surface layer and a constant value above. In the course of integration the profiles of the basic boundary layer variables demonstrate a nearly well mixed convective cloud topped boundary layer. The divergence of the longitudinal momentum transport associated with the subgrid-scale eddies and with the rolls reduces the mean vertical gradients of $\langle\bar{v}\rangle$-momentum in the boundary layer but produces a wind jump from the wind in the mixed layer to the geostrophical wind above. With respect to the mean lateral wind component we note that $\langle\bar{u}\rangle$-momentum is well mixed in the boundary layer and that the inflection point height lifts with time (occurring in the vicinity of the capping inversion) parallelling the boundary layer growth. Surface heating leads to the formation of a mixed layer near the sea surface, surmounted by a conditionally unstable cloud layer. This layer is capped by an inversion whose height grows in time (or with distance from the shoreline). The profile of the specific humidity shows a strong drop from saturation at the surface to a nearly constant value in the mixed layer and a linear decrease in the cloud layer. In addition, due to the surface moisture and heat flux the boundary layer is moistened and warmed reducing both, the moisture jump and the temperature difference between the sea surface and the overlying air. The mean liquid water content shown in Figure 4e has a peak value of about $1.6 \cdot 10^{-4}$ kg/kg at t = 7200 s. The cloud base is located at z = 250 m; from this height $\langle\bar{q}_l\rangle$ increases adiabatically up to 500 m. In the inversion zone $\langle\bar{q}_l\rangle$ is subadiabatic, which is a typical feature owing to the entrainment of dry air from above and the subsequent evaporation of cloud droplets. The cloud top cooling $(\partial\bar{\Theta}_l/\partial t)_R$ is distributed over a depth of about 250 m, which appears to be a rather deep layer, but seems to be reasonable realizing that $(\partial\bar{\Theta}_l/\partial t)_R$ represents a space-time average and that cloud top heights exhibit a wave-like undulation with differences in height up to 100 m. The maximum cooling rate of 2.4 K/h occurs at level z = 600 m, corresponding to the level of maximum liquid water content. This value is strongly dependent on the vertical mesh size and the cooling peak is localized near the surface of clouds. The fact that the ocean surface emits radiation at higher temperatures than the cloud is also seen in Figure 4f. It leads to a slight heating at the grid points shortly above the cloud base.

Important variables for describing the turbulence structure of any boundary layer, are the second order moments. Vertical profiles of resolved-scale horizontal and vertical velocity intensities as well as the variance of the resolved-scale virtual potential temperature fluctuations are shown in Figure 5a-5d at times t = 1800 s (solid), t = 4500 s (short-dashed) and at t = 7200 s (long-dashed). At t = 1800 s and at t = 4500 s

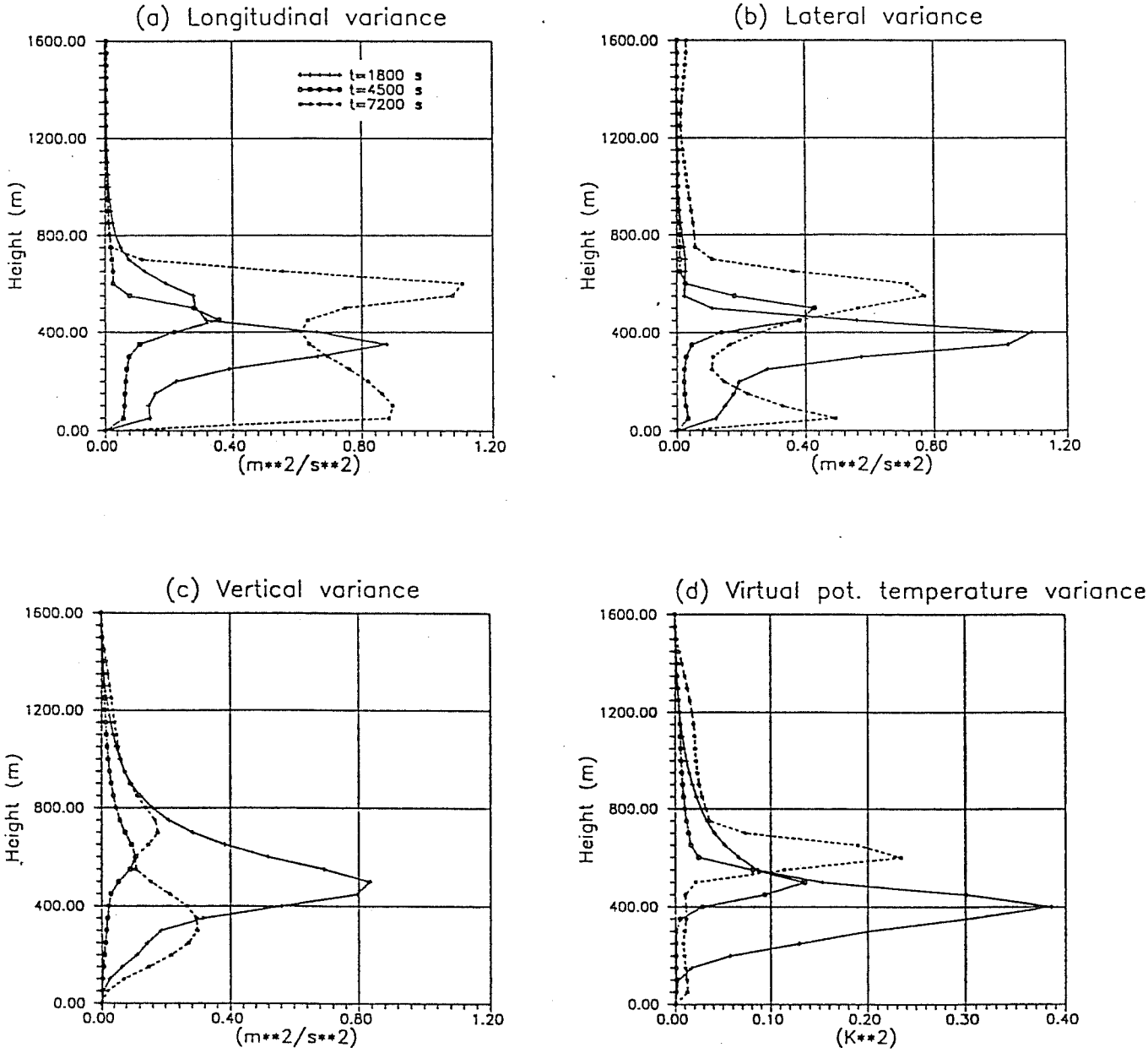

Fig.5: Profiles of resolved-scale variances of the longitudinal $\overline{v}''$ (a), of the lateral $\overline{v}''$ (b) and of the vertical velocity component $\overline{w}''$ (c) as well as of virtual potential temperature $\overline{\theta}_v''$ (d) for the control case at t = 1800 s (solid), t = 4500 s (short-dashed) and at t = 7200 s (long-dashed).

the profiles of $\overline{u}''$- and $\overline{w}''$-variance exhibit maxima in the upper part of the boundary layer, not far away from the inflection point in the mean lateral wind component, where the largest shear is present. These profiles are typical for situations in which shear generated vortices due to inflection point instability are met (e.g. Chlond, 1987). The longitudinal velocity variance $<\overline{v}''^2>$ is seen to maintain a nearly constant value in the mixed layer but shows a maximum near boundary layer top, which can partly be explained by the profile of $\overline{v}$: $\overline{v}''$ - variance is produced by the adjustment from $\overline{v}$ to v_g in the thin inversion layer. At t = 7200 s an absolute maximum of $\overline{w}''$-variance occurs in the middle of the boundary layer. This feature agrees with the idea that the rolls become increasingly more convective in character with distance from the shoreline. A relative maximum of $<\overline{w}''^2>$ again occurs near cloud top indicating mechanical energy production. The variance of the horizontal velocity fluctuations shows two maxima in the boundary layer. The first maximum occurs near the surface where the wind shear is important, and the second maximum again appears in the entrainment zone owing to the inflection point instability. In contrast to previous two-dimensional roll theories (e.g. that of Mason and Sykes (1982) or that of Chlond (1987)) but in accordance with the observations, the model predicts a resolved-scale variance ratio $<\overline{v}''^2>/<\overline{u}''^2>$ of the order one, while two-dimensional models predict a ratio of $<\overline{v}''^2>_{max}$ to $<\overline{u}''^2>_{max}$ between 4:1 and 10:1. This fact supports the suggestion that three-dimensional effects reduce the resolved-scale variance ratio $<\overline{v}''^2>/<\overline{u}''^2>$ because, as a result of the pressure-velocity-gradient correlation $<\overline{p}'' \partial\overline{v}''/\partial y>$, coupling of $\overline{v}''$-momentum to $\overline{u}''$-, and $\overline{w}''$-momentum is stronger than two-dimensional models suggest. The effect of this correlation is to produce a equipartition of resolved-scale energy since the transfer of energy, via pressure forces, is from the high-intensity to the lower intensity component.

The variance of the resolved-scale virtual potential temperature fluctuations is shown in Figure 5d. Temperature fluctuations are produced by the negative product of heat flux and temperature gradient. This product is large at the inversion but is small in the middle of the boundary layer. This explains the general shape of the profile, as in the mixed layer no large fluctuations are possible for air parcels displaced in the vertical direction. On the other hand, the $\overline{\Theta}''_v$-variance reaches a maximum at the inversion. This maximum is associated with the development of increased stratification at the inversion because in the entrainment zone even small vertical motions cause large fluctuations because of the strong vertical gradients there. This tendency has been confirmed from experimental and numerical studies for dry and moist convective boundary layers (e.g. Brümmer, 1985; Brümmer et al., 1992; Mason, 1989; and Sykes et al., 1990).

Vertical profiles of longitudinal and lateral momentum flux are shown in Figures 6a-6b. These profiles, as well as those given in the following figures, represent time averages and, except when indicated, the flux curves include the resolved-scale val-

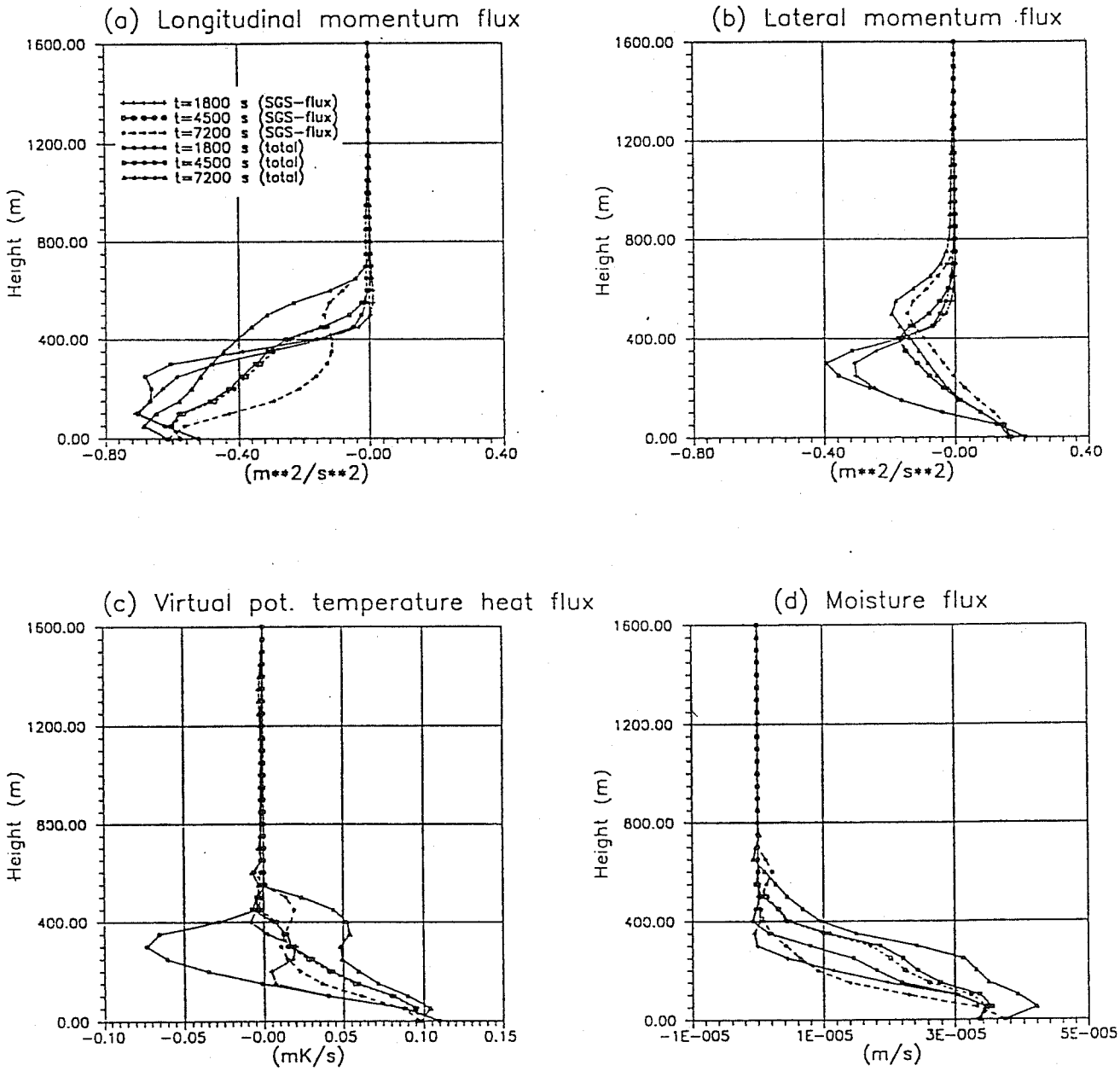

Fig.6: Profiles of total transports of longitudinal $<\overline{v'' w''}>$ (a) and lateral momentum $<\overline{u'' w''}>$ (b) as well as of virtual potential temperature $<\overline{w'' \theta_v''}>$(c) and water vapour $<\overline{w'' q_v''}>$ (d) for the control case. Parameterized subgrid-scale parts of the transports are shown by dashed lines. Other features as in Fig.3.

ues and their subgrid-scale counterpart. The calculated longitudinal momentum flux $\langle \overline{v''w''} \rangle$ has its maximum close to the sea surface and decreases rapidly with height to values near zero at the top of the boundary layer. At t = 1800 s and t = 4500 s the total downward longitudinal momentum flux is nearly entirely transported by the parameterized SGS-eddies whilst at t = 7200 s about 40% of the total longitudinal momentum flux existed on the sub-grid-scale at z = 200 m; this fraction dropped to about 20% for z > 300 m. The lateral momentum flux is generally smaller than the longitudinal one and the major contribution comes from the subgrid-scale. The flux decreases with increasing distance from the sea surface and shows a minimum in the upper half of the boundary layer. In the lower part of the boundary layer the divergence of this flux tends to increase $\bar{u}$-momentum and vice versa in the upper part. Therefore, the action of the lateral momentum flux divergence is to diminish the wind difference above and below the inflection point to relieve the vorticity maximum.

Figure 6c shows the profile of virtual potential temperature heat flux (buoyancy flux) together with the SGS-contribution. The buoyancy transport is nearly totally due to SGS mixing during the first 1.5 hours of integration except in the inversion zone where the resolved-scale fraction appears dominant. Afterwards a considerable part of the transport of virtual potential temperature was taken over by the resolved-scale eddies. At t = 7200 s the total buoyancy flux exhibits a typical structure. It is close to linear up to the cloud base and is caused by surface heating owing to the temperature difference between the sea surface and the overlaying air of about $\Delta\bar{\Theta} \approx$ + 2.9 K. The linear profile implies a constant heating rate in the mixed layer and is an indicator for the stationarity of the turbulent state in the mixed layer. Inside the cloud the virtual potential temperature heat flux increases to values of $\approx$ 50 W m^{-2} and attains a maximum in the middle of the cloud layer. Above it, the heat flux again decreases slowly throughout the upper cloud layer, changes sign at z = 600 m and becomes slightly negative in the inversion zone because warmer and dryer air from above is transported against thermal stability into the boundary layer (i.e. owing to entrainment). The maximum negative entrainment heat flux amounts to $\approx$-10W m^{-2}. The dashed curves represent the SGS contributions. At the surface, the resolved-scale vertical velocity vanishes and therefore, all the flux is transported by SGS contribution at this level. Above this level, the mean SGS flux is very small and becomes negative near the inversion. Our results show that there is a very substantial positive buoyancy flux in the upper part of the boundary layer. The reason for this is twofold. First, radiative cooling, which is most efficient at cloud top, leads to a positive buoyancy flux there for the same reason that heating at the bottom of the boundary layer leads to a positive buoyancy flux there, i.e. to compensate the loss of heat due to radiative cooling, a large positive heat flux is established inside the cloud. In addition, conversion of water vapour to liquid water releases latent heat and therefore, creates a positive buoyancy flux.

The water vapour flux (Figure 6d) was mainly due to boundary layer turbulence for the first phase of the cold air outbreak, before a substantial part of the water vapour transport was taken over by the resolved-scale roll circulation. The profile of moisture flux derived from the simulation is positive (i.e. directed upward) over the total area. Evaporation at the ocean surface increases the moisture content in the surface layer, which is then mixed by turbulence and the roll vortices to upper regions. Therefore, the flux has its maximum close to the sea surface and decreases with height to small positive values at the top of the boundary layer where boundary layer moisture is diluted by entrainment of dry environmental air. However, as this dilution is smaller than the import from the surface, the total amount of moisture increases in the whole boundary layer during the course of integration. At t = 7200 s the parameterized fraction of the moisture flux appears negligible except in the lower 150 m and at the top of the boundary layer.

In this subsection we consider in detail the mechanisms by which the rolls obtain energy and investigate how the dynamics of such convective structures depend upon the distance from the shoreline. Physical instability mechanisms leading to the occurrence of rolls are known. Roll vortices can be generated by buoyancy or by shear or a combination of the two. In order to identify the instability mechanisms responsible for the generation of rolls we examine the resolved-scale kinetic energy budget. In this way we quantify the processes in the production and maintenance of rolls. Production terms in the budget equation for resolved-scale turbulence energy $\langle E_R \rangle = 1/2 \langle \overline{u}''^2 + \overline{v}''^2 + \overline{w}''^2 \rangle$ are shown in Figure 7a and 7b as function of height at times t = 1800 s, t = 4500 s and t = 7200 s. Positive values contribute towards growth of $\langle E_R \rangle$ and negative values contribute towards decay. The production of roll kinetic energy by buoyancy $g/T_0 \langle \overline{w}'' \overline{\Theta}''_v \rangle$ describes the flow of energy from the reservoir of potential energy to roll kinetic energy by means of a positive heat flux whilst the shear production term $-\langle \overline{u}''\overline{w}'' \rangle d\langle \overline{u} \rangle/dz - \langle \overline{v}''\overline{w}'' \rangle d\langle \overline{v} \rangle/dz$ arises from the interaction of the Reynolds stress and the mean wind components. At t = 1800 s the strength of the shear term is apparent, especially at the 300 m height. This is not surprising considering the large wind shear in the mean lateral wind component at this height. Thus, we conclude that during the first phase of the cold air outbreak the rolls are produced by dynamic (inflection point) instability which corresponds to the dynamic energy source for rolls as described by Brown (1970). As seen in Figure 7b a great portion of this energy gain is converted into potential energy by buoyant destruction of energy since the rolls have to perform work against stable stratification (i.e. a great portion of shear generated turbulence is used to lift the boundary layer by entrainment of warm stable environmental air from above). At t = 4500 s the shear stress as well as the buoyancy production terms are seen to be rather small indicating a transition stage. At a greater distance from the shoreline (i.e. at t = 7200 s) there exists a broad maximum in the buoyancy production in the sub-cloud and

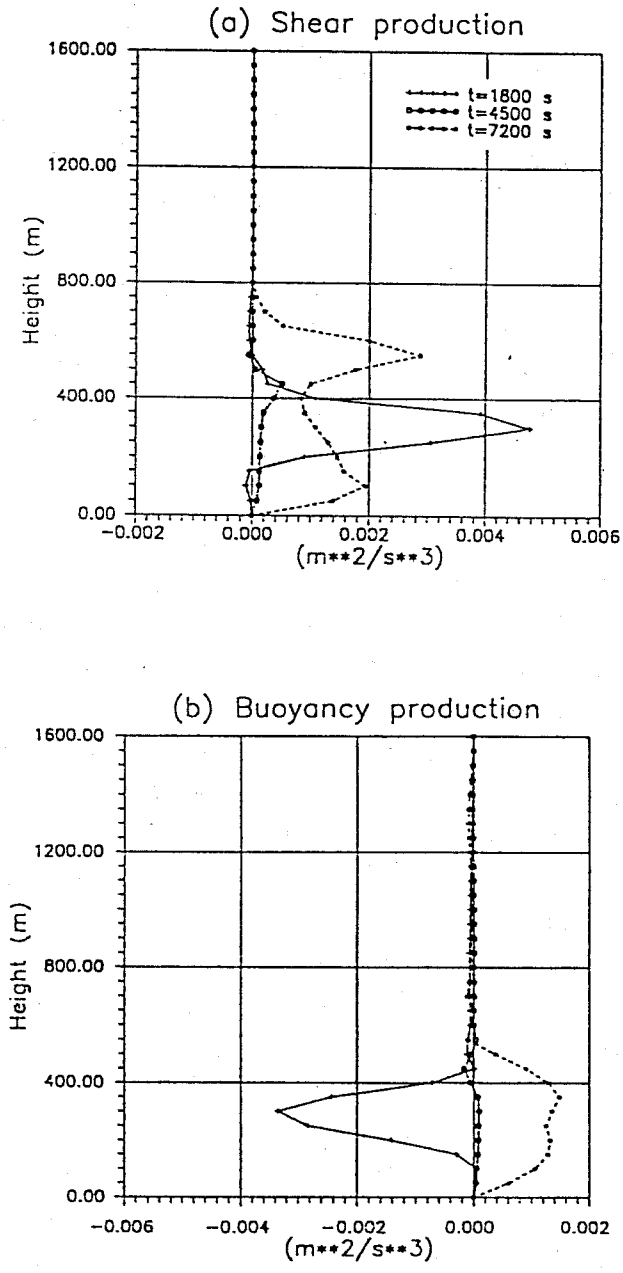

Fig.7: Average profiles of the energy production of resolved-scale turbulence energy $\langle E_R \rangle = 1/2 \langle \overline{u}^2 + \overline{v}^2 + \overline{w}^2 \rangle$ by wind shear of the basic flow $\left(- \langle \overline{v}''\overline{w}'' \rangle d\langle \overline{v} \rangle/dz - \langle \overline{u}''\overline{w}'' \rangle d\langle \overline{u} \rangle/dz \right)$ (a) and by buoyancy $\left(g/\Theta_o \langle \overline{w}''\overline{\Theta}_v'' \rangle\right)$ (b) for the control case. Other features as in Fig.3.

cloud-layer, suggesting that buoyancy is now the main driving force for the rolls. The shear production term is seen to have been rather unimportant in the middle part of the boundary layer, but turns out to be the dominant in the resolved-scale turbulent energy equation near the ground and near the inversion. Our results show a good qualitative correspondence with measured values of the kinetic energy production terms which are based on FALCON profile soundings on 16 May 1988. As can be seen in Figure 8 the observations also support the idea that the secondary flow structures are formed by dynamic processes during the first phase of the cold air outbreak and that the thermal convection becomes dominant later on. However, there are some discrepancies between the observations and the simulated results. In particular, the model tends to overestimate the magnitude of the energy generation terms. This apparent discrepancy may at least partly traced back to the fact that the measured fluxes only include contributions from motions with horizontal scales up to 1 km whilst the model results comprehend contributions from motions with horizontal scales up to 6 km. In summary, inspection of the generation terms in the roll kinetic energy budget equation permits to quantify the processes leading to the formation of rolls. We found that during the first phase of the cold air outbreak the rolls were produced by dynamic instability in the presence of strong vertical wind shear but became increasingly more convective in character with distance from the shoreline owing to convective instability supplying energy at the roll wavelength. However, the large value of the shear stress term at the top of the boundary layer leads us to conclude that dynamic instability is still playing an important role in determining the roll structure during the later stage.

3.3. Sensitivity Runs

In order to examine the sensitivity of the simulated roll vortices to various physical processes, sensitivity tests were performed. The control case was re-run with

a. a large-scale mean subsidence (Run 1 with $w_{LS} = -10^{-2}$ ms^{-1} at $z = z_{TOP} = 1600$ m)
b. no time dependent surface heating (Run 2 with $(\partial\overline{\Theta}_l/\partial t)_{z=z_0} = 0$)
c. a modified large-scale moisture field (Run 3 with $\Gamma_q = -1.079 \cdot 10^{-6}$ m^{-1} corresponding to a linear decrease of the total water content q with height at time t = 0 s from $\overline{q} = 2.2 \cdot 10^{-3}$ kg/kg at z = 25 m to $\overline{q} = 0.5 \cdot 10^{-3}$ kg/kg at z = 1600 m)
d. no long-wave radiative effects (Run 4) and with
e. latent heating due to condensation and evaporation artificially turned off (Run 5)

in order to asses the importance of these effects.

Figure 9 shows vertical profiles of resolved-scale vertical velocity variance (a), resolved-scale virtual potential temperature heat flux (b), and of mean liquid water

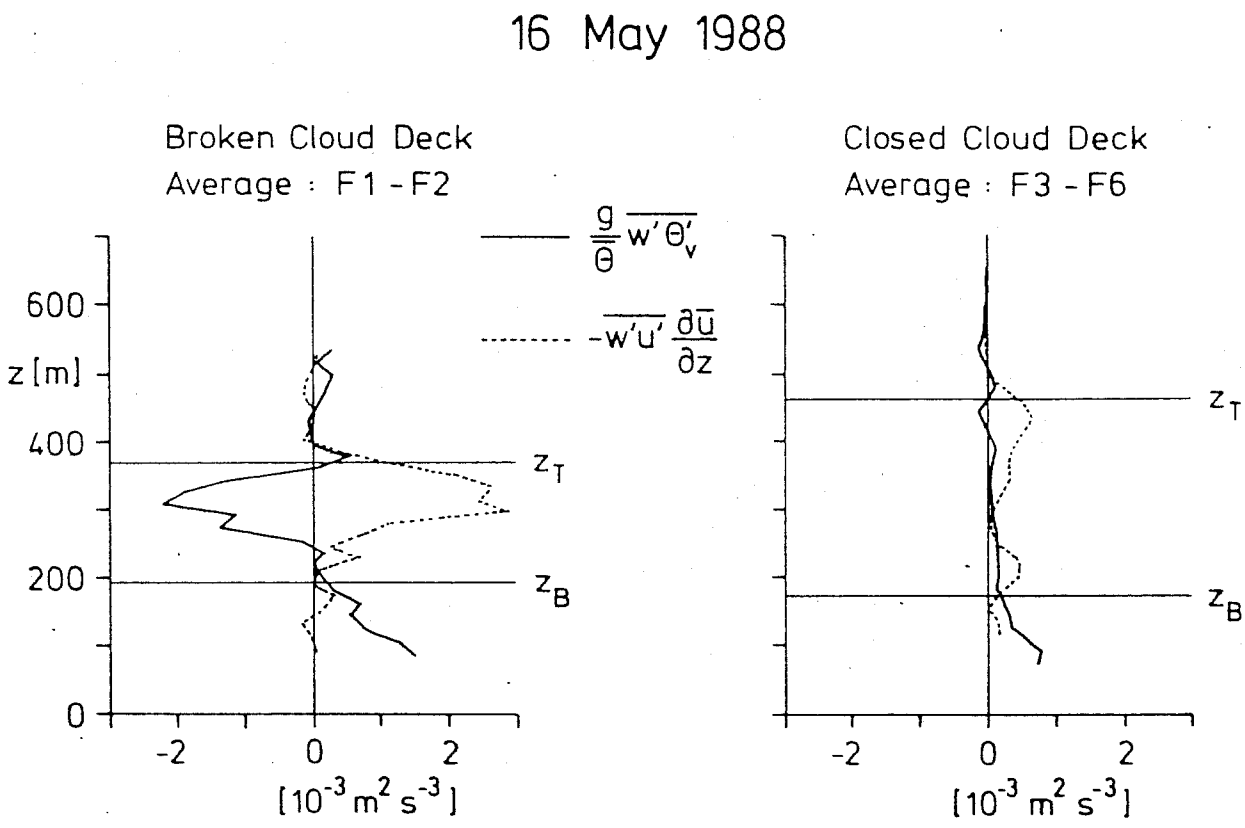

Fig.8: Profiles of kinetic energy production by wind shear of the basic flow - $\overline{u'w'}$ and by buoyancy $g/\bar{\theta}\,\overline{w'\theta'}$ derived from 1 km long horizontal subsections of the FALCON profile flights on 16 May 1988. Profiles in the left panel represent averages in the region with broken clouds and the profiles in the right panel are averages in the region with a closed cloud deck. The averages are performed relative to cloud base zB and cloud top zT to maintain characteristic structures (after Brümmer et al., 1992).

content (c) for the different runs at time t = 7200 s during the convective regime. This time period has been chosen because the boundary layer profiles for the mean quantities (apart from changes in boundary layer temperatures and moisture contents in Runs 2 and 3 arising from different initial and boundary conditions) and for the second order moments appear very similar for the various cases during the first 1.5 hours of integration time. Full lines are used to denote the results of the control run whilst dashed line patterns are used to label the results of the sensitivity runs.

As seen in Figure 9a the omission of surface warming, latent heat release, radiative cooling or large-scale subsidence or less water vapour all produce less vigorous boundary layer eddies. The greatest reductions in the vertical velocity intensity occur in Runs 3 and 5 where $<\overline{w}">^2_{max}$ has dropped from 0.3 m^2s^{-2} to 0.12 m^2s^{-2} and to 0.13 m^2s^{-2}, respectively. The physical reason for this effect is the lowered cloud activity (Run 3) and the absence of the energy source (Run 5) due to latent heat release, respectively. In Run 3 owing to the initial decrease of the total water content with height entrainment of relatively drier air from the region just above the inversion tends to dry out the boundary layer resulting in a conversion rate from water vapour to liquid water (and hence a heat release) which is much less than in the reference run. Therefore, condensation is providing a significant energy source causing more intense boundary layer eddies. This feature agrees with the idea that ascending buoyant plumes receive an additional vertical impulse due to heat release. Moreover, Figure 9a depicts that the lack of significant cloud top cooling (Run 4), the absence of time dependent surface heating (Run 2) as well as a large-scale subsidence also severely weakened the system as a whole. The comparison reveals a drastic decrease of vertical velocity intensity $<\overline{w}">^2_{max}$ (0.14 m^2s^{-2} (Run 4), 0.15 m^2s^{-2} (Run 2) and 0.22 m^2s^{-2} (Run 1) versus 0.30 m^2s^{-2} in the control run).

The (de)-stabilizing effect of the various physical processes investigated is also reflected in the profiles of virtual potential temperature heat fluxes (Figure 9b). In the case of large-scale subsidence (Run 1) and in the absence of time dependent surface heating (Run 2) the buoyancy flux shows a uniform decrease of 10% and of 40% at all levels, respectively. The great reduction of the virtual potential temperature heat flux in the case of a spatial homogeneous ocean surface temperature is reasonable realizing that due to the input of heat at the ocean surface the boundary layer is warmed with the downwind distance from the shoreline, thereby diminishing the air-sea temperature difference. In the control run the latitudinal temperature variation of the ocean surface partly counterbalances the boundary layer warming. As a consequence, a much higher surface heat flux is obtained in the control run (100 Wm^{-2} versus 60 Wm^{-2}) than in Run 2 leading to more unstable conditions in the surface layer. The surface layer instability is therefore seen as a feature which enhances the ability of the cloud circulation to "pull" air upwards and to influence the overall potential energy of the atmosphere due to enhanced vertical convective transports.

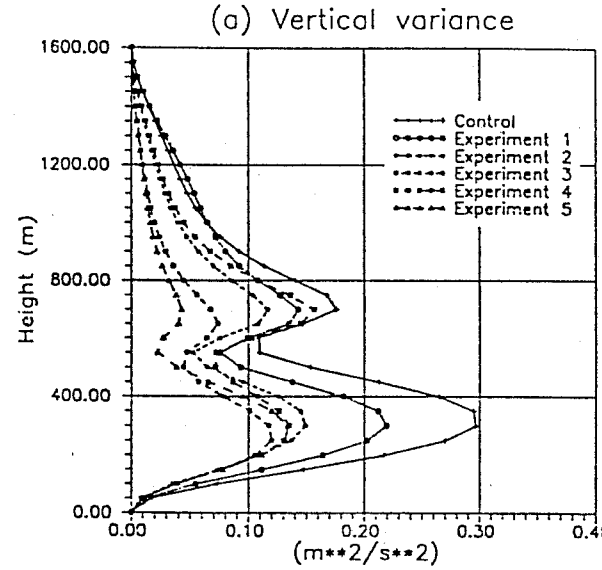

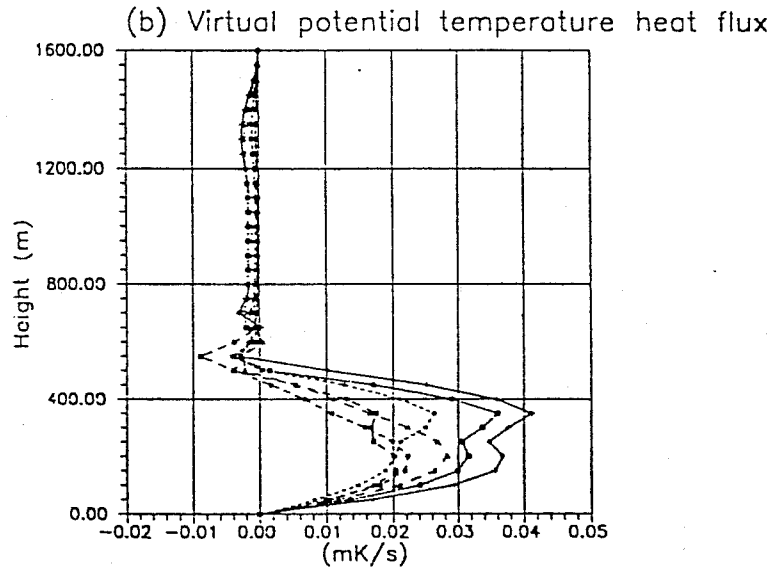

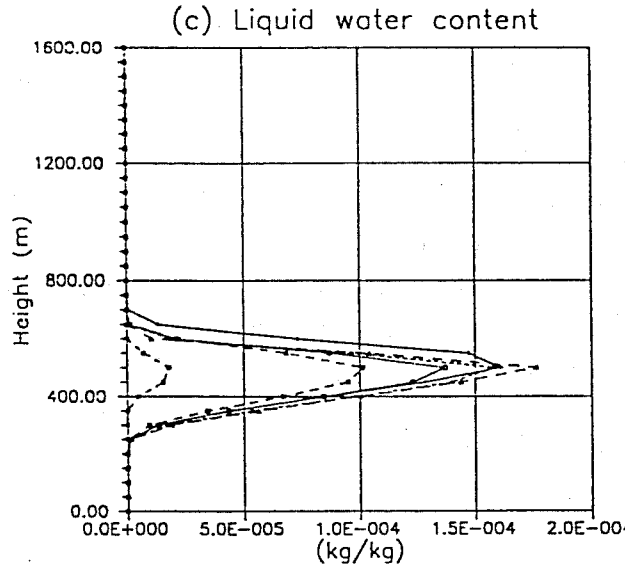

Fig.9: Average profiles of resolved-scale vertical velocity variance (a) of resolved-scale virtual potential temperature heat flux (b) and of the liquid water content at t = 7200 s for Runs 1 - 5 and the control run.

The reduced surface instability in Run 2 cuts off part of the internal energy input into the model atmosphere, and thus a less vigorous roll circulation is found after 2 hours of integration time. Smaller values of the buoyancy fluxes are also found in the sensitivity Runs 3 and 5, especially in the upper part of the boundary layer because as explained in the preceding paragraph the convectively generated updrafts do not provide a corresponding latent heat release. Radiation effects have not been included in many studies of the convective boundary layer (e.g Sykes et al., 1988; Raasch, 1990). The underlying assumption was that the surface fluxes should dominate the boundary layer development, justifying the neglect of radiation. However, our numerical simulation of boundary layer vortices (Run 4) has revealed a surprising sensitivity to longwave radiative cooling/heating. We find that longwave radiation from the cloud top can produce strong cooling and hence significantly influence the dynamics of clouds. The effect of radiative cooling is twofold. First, the long-wave radiative flux divergence existing in the entrainment zone will serve to cool the cloudy air in that zone and therefore, promote entrainment by reshaping the temperature profile there (Kahn and Businger, 1979, refer to this process as "direct" entrainment). Second, that part of the radiative flux divergence concentrated below the entrainment zone (i.e. within the upper cloud layer inside the convective boundary layer) will, on the other hand, produce kinetic energy just as does heating at the ground and will, therefore, be one of the driving mechanisms of the boundary layer turbulence. Our calculation reveals that the latter process is of primary importance in the model atmosphere. We find that the increase of resolved-scale vertical variance in the control run (including radiation) is linked to an increase in the vertical flux of virtual potential temperature, which is one of the main sources of kinetic energy. Compared to Run 4 this quantity is at time t = 7200 s approximately doubled in the control run inside the cloud layer (see Figure 9b). Therefore, we conclude that in the case of the convective boundary layer during cold air outbreaks the cloud radiation interaction increases cloud activity and related turbulent quantities due to destabilization of the cloud layer.

The impact of the absence of cloud top cooling is also documented in Figure 9c showing profiles of the liquid water content. The lack of radiative effects has severely weakened the system as a whole. The peak liquid water content has dropped from 0.16 g/kg to 0.10 g/kg and the fractional cloud cover is smaller (0.80 versus 1.00) than in the reference case. In comparing liquid water contents and fractional cloud cover from Runs 1, 2 and 5 with those of the control run we find that the large-scale subsidence, the absence of time dependent surface heating and the lack of latent heating have only a small influence upon cloud structure. For example, as a consequence of warming the convective boundary layer, large-scale subsidence leads only to a weak reduction in the liquid water content (0.14 g/kg versus 0.16 g/kg) and in the fractional cloud cover (0.97 versus 1.0). In contrast, a large-scale vertical moisture gradient (Run 3) produces dramatic changes in liquid water and the whole

boundary layer structure. In this case the entrainment of warmer and drier air from aloft prevents the formation of a complete cloud cover. Therefore, the gradient in the $\bar{q}$-profile results in a drying of the boundary layer which is documented by lifting of the cloud base (350 m versus 250 m) relative to that seen in the control run. In addition, the resulting fractional cloud cover is by far smaller than in the reference case (0.32 versus 1.00) and the peak area averaged liquid water content has dropped from 0.16 g/kg to 0.018 g/kg.

Figure 10 shows realizations of the vertical velocity and the liquid water content fields for Run 3 in horizontal (at z = 500 m) and vertical (at y = 3200 m) plan views at time t = 7200 s. The flow field consists of much more regular and steady eddies than those of the control run. The flow is again dominated by boundary layer rolls with a wavelength of about 1070 m. The updrafts have about the same width than the downdrafts. The maximum concentrations of the liquid water content are located near the top of the strongest updrafts and move steadily from right to left in the illustrations shown in Figure 10. There is a tendency for clouds to trail behind the updrafts. The lower relative humidity in the free atmosphere (owing to the prescribed initial decrease of the total water content in Run 3) results in a reduced cloudiness in the boundary layer relative to that seen in the control run. Thus, the basic mechanism sustaining the cloud free areas between the updrafts is the mixing of saturated moist cloud air with overlying warmer and drier air. This indicates that under certain environmental conditions an individual cloud is capable of drying out a large area of the surrounding layer through cloud top entrainment and thus is able to produce significant gaps between the clouds. Therefore, these results suggest that the large-scale vertical moisture gradient indeed has a strong influence on the cloud morphology as well as on the turbulence structure of the convective boundary layer during cold air outbreaks.

4. Conclusions

Results of three-dimensional numerical calculations of boundary layer roll vortices for a variety of conditions have been presented. Here we have adopted the numerical technique of Large-Eddy-Simulation (LES) to the cloud topped convective boundary layer, i.e. the numerical model explicitly calculates the spatial averages which represent the dominant large-scale motions whilst the effect of the smaller scale (subgrid) motions on the averaged quantities is parameterized. The main progress regarding previous modelling effort has been to fully take into account three-dimensional circulations and to include most of the physical processes occurring in a moist boundary layer. Apart from the aspects of the turbulence closure three main physical processes have been taken into account: a water cycle (including a subgrid scale condensation scheme), infrared radiative cooling in cloudy conditions and the perturbations of the

RUN 3

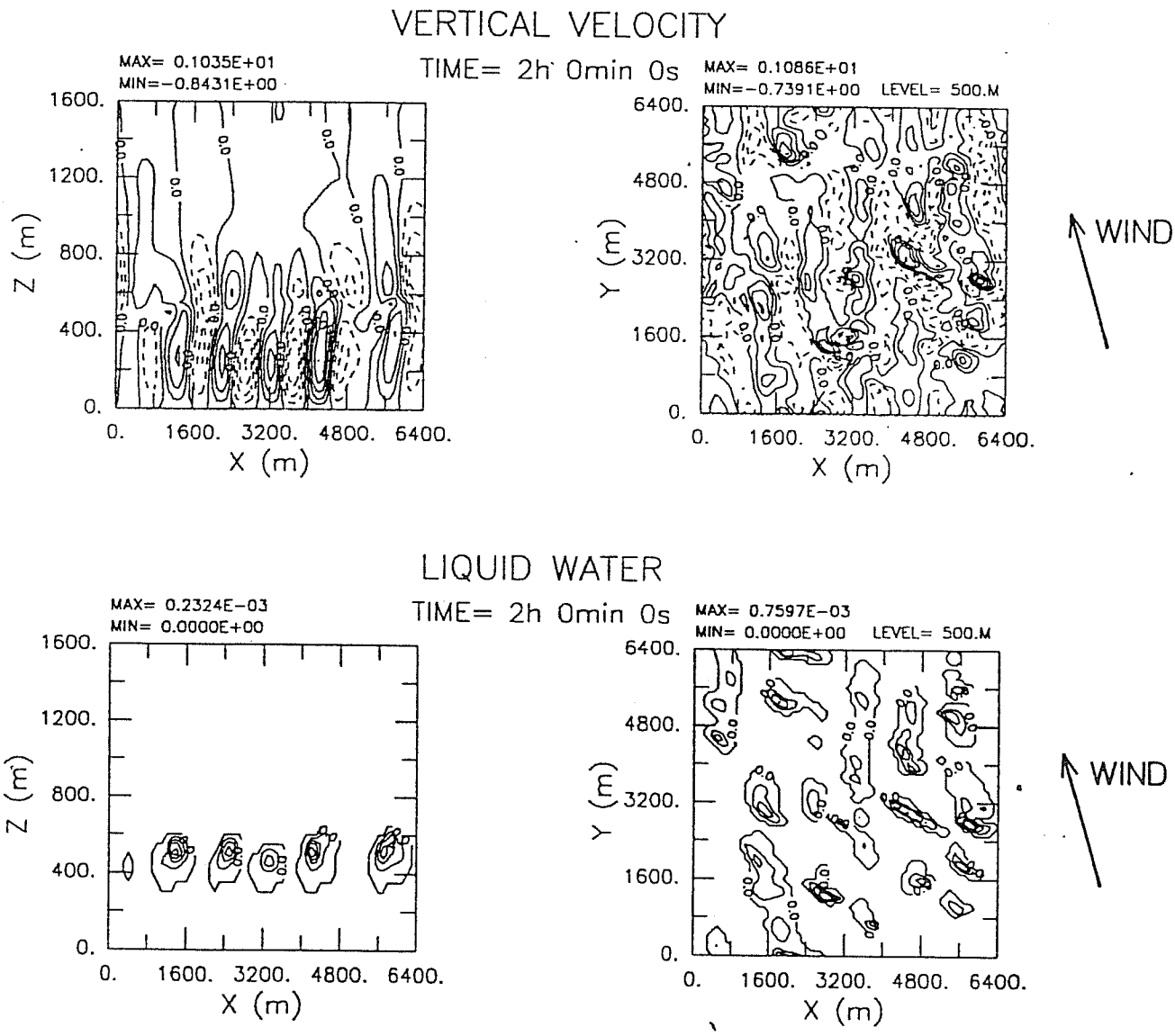

Fig.10: Realizations of the vertical velocity (top panel) and the liquid water content fields (bottom panel) in vertical (at y = 3200 m) and horizontal plan views (at z = 500 m) for Run 3 at t = 7200 s.

local fields by large-scale subsidence.
As a principal conclusion, it can be stated that the three-dimensional simulation of the boundary layer eddy structure under conditions approximating those of the cold air outbreak of a particularly interesting case of ARKTIS 1988 (16 May 1988) exhibit a cloud structure similar to that observed. Though in some respects the model simulations differ from the ARKTIS actual meteorological situations, typical characteristics of the dynamics of the boundary layer flow during cold air outbreaks are revealed by the model. These include: (1) the boundary layer grows rapidly as the cold air flows off the ice over the relatively warm water; (2) organized structures in the form of quasi-two-dimensional roll vortices are identified in this boundary layer; (3) apart from the entrainment zone, vertical transports of heat and moisture are due to subgrid-scale turbulence for the first phase of the cold air outbreak, before the rolls cause a substantial mixing of these quantities as the boundary layer deepens; (4) cloud streets with a wavelength of about 2 km are formed 40 km or less downstream from the shoreline. The cloud layer thickens quite rapidly with the downwind distance from the coast and forms a nearly continuous cloud layer at a distance of about 100 km from the ice edge, in which the rolls can be identified as rows of denser clouds; (5) roll vortices that form at the beginning have different characteristics than those that appear later on.

The discussion on the mechanisms by which the rolls obtain energy clarified the relative importance of the various physical processes in the production and maintenance of rolls. We found that during the first phase of the cold air outbreak the rolls forming within the boundary layer are mainly driven by a dynamic instability in the presence of a strong vertical wind shear but become increasingly more convective in character with distance from the shoreline owing to the thermal instability supplying energy at the roll wavelength.

Attention has been given to the dependence of the results upon various physical processes and factors influencing the simulations: large-scale subsidence, time dependent surface heating, a large-scale vertical moisture gradient, radiation and latent heat release. Based on the sensitivity simulations the following conclusions can be drawn:

- Realistic values of large-scale subsidence are too small to allow more than a small influence on the cloud topped convective boundary layer. Large-scale subsidence results in a slight decrease in cloud liquid water contents and resolved-scale energy levels.
- As a consequence of a spatially homogeneous ocean temperature, a lowered surface layer instability reduces the kinematic surface heat flux and thus a less vigorous roll circulation is found after two hours of integration time.
- The presence of a large-scale vertical moisture gradient prevents the formation of a complete cloud cover. In this case clouds form only in the updrafts of the

dominant rolls. The key ingredient for such an organization appears to be the decrease in equivalent potential temperature at the top of the boundary layer in conjunction with the ability of clouds to entrain warm, dry air from aloft in order to give significant gaps between the cloud streets. Therefore, our calculations give grounds for believing that the structure of the initial moisture field indeed has a strong influence on the cloud morphology and ultimately controls the fractional cloud cover.

- The major feature of radiative forcing is seen to be strong cloud-top cooling. This leads to enhanced destabilization of the upper cloud layer, which in turn results in an increased cloud activity and related turbulent quantities.
- Latent heating due to condensation provides a significant energy source causing more intense boundary layer eddies.

Although the results in this study refer to only one case of boundary layer modification in a cold air outbreak, we think that our simulation may serve as an instructive example giving insight into different interacting physical processes. In addition, the sensitivity simulations undertaken as a test of the response of the model to a change in a significant physical process or parameter indicate that the model is indeed responding in a physically plausible manner. Such sensitivity tests are in fact one of the principal objectives of numerical models, and make those a powerful tool to provide insight into the underlying dynamics.

References

Brown, R.A. (1970): A secondary flow model for the planetary boundary layer. J. Atmos. Sci., 27, 742-757.

Brown, R.A. (1980): Longitudinal instabilities and secondary flows in the planetary boundary layer: A review. Rev. Geophys. Space Phys., 18, 683-697.

Brümmer, B. (1985): Structure, dynamics and energetics of boundary layer rolls from KonTur aircraft observations. Contr. Atm. Phys., 58, 237-254.

Brümmer, B., Rump, B., and Kruspe, G. (1992): A cold air outbreak near Spitsbergen in springtime: Boundary layer modification and cloud development. Boundary-Layer Meteorol., 61, 13-46.

Chlond, A. (1987): A numerical study of horizontal roll vortices in neutral and unstable atmospheric boundary layers. Contr. Atm. Phys., 60, 144-169.

Chlond, A. (1992): Three-dimensional simulation of cloud street development during a cold air outbreak. Boundary-Layer Meteorol., 58, 161-200.

Cox, S.K. (1976): Observation of cloud infrared effective emissitivity. J. Atmos. Sci., 33, 287-289.

Deardorff, J.W. (1972): Numerical investigation of neutral and unstable planetary boundary layers. J. Atmos. Sci., 29, 91-115.

Deardorff, J.W. (1980): Stratocumulus - capped mixed layers derived from a three-dimensional model. Boundary-Layer Meteorol., 18, 495-527.

Etling, D., and Raasch, S. (1987): Numerical simulation of vortex roll development during a cold air outbreak. Dyn. Atmos. Oceans, 10, 277-290.

Hein, P.F., and Brown, R.A. (1988): Observations of longitudinal roll vortices during arctic cold air outbreaks over open water. Boundary-Layer Meteorol., 45, 177-199.

Herring, J.R. (1979): Subgrid scale modeling - an introduction and overview. Turb. Shear Flows, 1, 347-352.

Kahn, P.H., and Businger, J.A. (1979): The effect of radiative flux divergence on entrainment of a saturated convective boundary layer. Quart. J. Roy. Met. Soc., 105, 303-305.

Küttner, J.P. (1971): Cloud bands in the atmosphere. Tellus, 23, 404-425.

LeMone, M.A. (1973): The structure and dynamics of horizontal roll vortices in the planetary boundary layer. J. Atmos. Sci., 30, 1077-1091.

Mason, P.J., and Sykes, R.I. (1982): A two-dimensional numerical study of horizontal roll vortices in an inversion capped planetary boundary layer. Quart. J. Roy. Met. Soc., 108, 801-823.

Mason, P. J. (1985): A numerical study of cloud streets in the planetary boundary layer. Boundary-Layer Met., 32, 281-304.

Mason, P.J. (1989): Large - eddy simulation of the convective atmospheric boundary layer. J. Atmos. Sci., 46, 1492-1516.

Mellor, G.L., and Yamada, T. (1974): A hierarchy of turbulence closure models for planetary boundary layers. J. Atmos. Sci., 31, 1791-1806.

Miura, Y. (1986): Aspect ratios of longitudinal rolls and convection cells observed during cold air outbreaks. J. Atmos. Sci., 43, 26-39.

Piasek, S.A., and Williams, G.P. (1970): Conservation properties of convection difference schemes. J. Comput. Phys., 6, 392-405.

Raasch, S. (1990): Numerical simulation of the development of the convective boundary layer during a cold air outbreak. Boundary - Layer Met., 52, 349-375.

Schumann, U, and Friedrich, R. (Eds.) (1986): Direct and large eddy simulation of turbulence. Notes on Numer. Fluid Mech., Vol. 15, Vieweg, Braunschweig.

Slingo, A. (1990): Sensitivity of the Earth's radiation budget to changes in low clouds. Nature, 343, 49-51.

Sommeria, G. (1976): Three-dimensional simulation of turbulent processes in an undisturbed trade wind boundary layer. J. Atmos. Sci., 33, 216-241.

Sommeria, G., and Deardorff, J.W. (1977): Subgrid-scale condensation in models of nonprecipitating clouds. J. Atmos. Sci., 34, 344-355.

Stephens, G.L. (1978): Radiation profiles in extended water clouds. Part II: Parameterization schemes. J. Atmos. Sci., 35, 2123-2132.

Sykes, R.I., Lewellen, W.S., and Henn, D.S. (1988): A numerical study of the development of cloud street spacing. J. Atmos. Sci., 45, 2556-2569.

Sykes, R.I., Lewellen, W.S., and Henn, D.S. (1990): Numerical simulation of the boundary-layer eddy structure during the cold-air outbreak of GALE IOP2. Mon. Wea. Rev., 118, 363-374.

Walter, B.A. (1980): Wintertime observations of roll clouds over the Bering Sea. Mon. Wea. Rev., 108, 2024-2031.